

# High performance multicrystalline silicon: grain structure and iron precipitation

Antoine Autruffe<sup>1\*</sup>, Mohammed M'hamdi<sup>1,2</sup>, Florian Schindler<sup>3</sup>, Friedemann D. Heinz<sup>3,4</sup>, Kai Erik Ekstrøm<sup>1</sup>, Martin C. Schubert<sup>3</sup>, Marisa Di Sabatino<sup>1</sup>, Gaute Stokkan<sup>5</sup>

<sup>1</sup> NTNU, Department of Materials Science and Engineering, Alfred Getz vei 2B, Trondheim, Norway

<sup>2</sup> SINTEF, Materials and Chemistry, Oslo, Norway

<sup>3</sup> Fraunhofer Institute for Solar Energy Systems ISE, Freiburg, Germany

<sup>4</sup> Freiburger Materialforschungszentrum FMF, Freiburg, Germany

<sup>5</sup> SINTEF, Materials and Chemistry, Trondheim, Norway

\*Corresponding author: Tel: +47 451 26 304, E-mail: [antoineautruffe@yahoo.fr](mailto:antoineautruffe@yahoo.fr)

**Abstract:** A study of the spatial occurrence of iron precipitation in a high performance multicrystalline silicon sample is presented. The separated effects of grain-boundaries, sparse intra-granular dislocations, and dislocation clusters are investigated by combining the Fe<sub>i</sub> imaging method with glow discharge mass spectroscopy, electron backscatter diffraction and two iron precipitation models. While the area-averaged precipitation at grain boundaries is relatively minor, almost the whole iron precipitation occurs within the grains, despite the very low intra-granular dislocation density. The fraction of non-precipitated iron in the studied HPMC-Si material was found to be one to two orders of magnitude higher than reported previously for standard materials.

**Keywords:** Multicrystalline silicon, extended defects, iron, precipitation.

## I. Introduction

Multicrystalline silicon is, together with monocrystalline silicon, the most widely used material in the photovoltaic industry. It contains a high density of extended defects, i.e. grain boundaries and dislocations, and a wide range of impurities, affecting the output solar cell performance. Iron has been identified as one of the most detrimental impurities in multicrystalline silicon [1, 2], and is found in relatively high concentration in ingots, originating from the crucible, its coating and the silicon feedstock [3-7]. Iron is present in silicon in the interstitial state or in the form of metal silicide nano-precipitates, mainly identified as FeSi<sub>2</sub> [8]. Previous studies have shown that a large majority of iron present in as-grown multicrystalline materials is precipitated [2, 9, 10]. Iron precipitation has a positive impact on the as-grown wafer quality, as the recombination activity of a precipitate per iron atom is generally considered being lower than the recombination activity of an isolated interstitial iron atom [2]. Iron precipitation at extended defects is, however, a strong limitation to the phosphorous gettering

efficacy [11], as only the mobile dissolved iron atoms have the ability to segregate towards the emitter.

Due to its relatively high solid diffusivity, iron precipitates mostly at extended defects [8]. Those defects present favorable precipitation sites and act as internal gettering sites during the ingot cooling. Recent improvements in the silicon growth technology have led to the solidification of multicrystalline silicon ingots of higher quality, i.e. with lower densities of dislocation clusters [12, 13]. This newly developed material is commonly referred to as high performance multicrystalline silicon (HPMC-Si), and presents a smaller grain size and a higher proportion of random angle grain boundaries compared to conventional multicrystalline silicon [14]. The precipitation behavior of iron is affected by the structure evolution of multicrystalline silicon, and it is of major interest to evaluate and predict the influence of each type of extended defects.

This study presents an examination of the spatial occurrence of iron precipitation during the cooling of an HPMC-Si ingot, and aims at investigating the separated effects of grain-boundaries, sparse intra-granular dislocations, and dislocation clusters.

## **II. Experimental Details**

The material investigated in this study has been grown in a pilot-scale Crystalox DS 250 furnace. The ingot was solidified in a fused silica crucible coated with silicon nitride. Polysilicon chips were used as feedstock, and the ingot was multi-seeded by melting only partially the feedstock. A more random structure – commonly referred to as high-performance multicrystalline silicon (HPMC-Si) – is obtained. The temperature profile resembles those typically used in industrial settings. The feedstock partial-melting was performed at a susceptor plateau-temperature of 1808 K, maintained during 170 minutes. The cooling rate, CR, used later for the calculations, was  $-2.73 \times 10^{-2}$  K/s. The final ingot was cut into nine 50x50x105 mm blocks. The central one was wafered, and the sample investigated in this study was taken at ~80% ingot height. Due to its high position in the ingot, the studied material contains more iron than typical wafers sampled in the middle of the ingot. This material selection is mainly justified by the detection limit of the chemical analysis method used for this study (glow discharge mass spectroscopy), and the influence of the total iron concentration is discussed at the end of Part.IV.B.

The selected wafers were first prepared using standard damage-etching and cleaning process. These steps occur at low temperatures. The grain structure was characterized by electron backscatter diffraction (EBSD) and a sister-wafer was used to evaluate the intra-granular dislocation densities. It was polished, Sopori-etched [15], and examined with light microscopy. The evaluation of the intra-granular dislocation density across the wafer was performed by averaging dislocation densities measured within 20 different grains, where the examined regions were located at least 0.1 cm away from the grain boundaries.

The wafers were passivated prior to the interstitial iron concentration measurements, by depositing an a-Si:H layer on both sides. This process lasted approximately 10 minutes, and the material was heated up to a maximum temperature of 230 °C. The samples were then annealed in a belt furnace at 450 °C within 1 minute. The influence of these two steps on the distribution of iron can be neglected with regard to the temperature history of the solidification process. Iron in its interstitial form,  $Fe_i$ , was quantitatively imaged on wafers by using an indirect technique based on carrier lifetime measurements [16, 17], performed by PL-imaging [18, 19]. The sample was firstly placed on a hot plate at 80 °C during 15 minutes to form FeB pairs. The charge carrier lifetime in the FeB state was then measured using a 790 nm diode laser at low injection level (0.1 suns). The sample was subsequently illuminated at maximum intensity during 4 minutes to split the FeB pairs, and the  $Fe_i$  dominated lifetime image was acquired at low injection level.  $Fe_i$  was then calculated according to the procedure suggested by Macdonald [16].

The total iron content  $C_0$  in the wafer was measured on a sister wafer by glow discharge mass spectroscopy (GDMS). The GDMS instrument used for this study has a detection limit for iron in silicon of 0.5 ppba – i.e.  $2.5 \times 10^{13} \text{ cm}^{-3}$  [20].

### III. Iron precipitation models

In order to discuss the relative impact of the different defects on iron precipitation, two types of precipitation models have been used:

- An area-averaged model.
- A 1D model accounting for both intra-granular and grain boundary precipitation.

These models are time dependent and aim at simulating iron precipitation during the ingot cooling.

The set of assumptions and equations used for the models are based on Ham's law [21], where all the precipitates are modeled as spheres, and the density of precipitation sites does not vary over time. It is initially assumed that precipitation starts right when the solubility limit is overcome, but as presented later, an adjustment has been made to account for the required supersaturation. The input parameters of the models are the densities of precipitation sites. A distinction is made between the intra-granular density of precipitation sites  $N_p^{IG}$  ( $\text{cm}^{-3}$ ), the surficial density of precipitation sites at a grain boundary  $N_p^{GB}$  ( $\text{cm}^{-2}$ ), and the area-averaged density of precipitation sites  $\overline{N_p}$  ( $\text{cm}^{-3}$ ).

#### A. Area-averaged precipitation

The area-averaged evolution of the dissolved iron concentration across the wafer  $\overline{C_i}$  is calculated from Equation (1).

$$\frac{\partial \overline{C}_i}{\partial t} = -\frac{\partial \overline{C}_p}{\partial t} = 4\pi r_p \overline{DN}_p (C_{sol} - \overline{C}_i) \quad (1)$$

where  $\overline{C}_p$  is the area-averaged concentration of precipitated iron,  $r_p$  is the average precipitate radius,  $\overline{N}_p$  is the area-averaged density of precipitation sites,  $D$  is the diffusivity of iron in solid silicon, and  $C_{sol}$  the solubility of iron in solid silicon. The average precipitate radius varies over time and is

$$r_p = \left( \frac{3 \overline{C}_p}{4\pi \overline{N}_p C_{Fe/FeSi_2}} \right)^{1/3} \quad (2)$$

$C_{Fe/FeSi_2}$  being the iron concentration in a  $FeSi_2$  precipitate.

### B. Grain boundary and intra-granular precipitation

The 1D model is solved numerically and the transport of iron is calculated using the 1D diffusion equation, adjusted for the case of diffusion-limited precipitation:

$$\frac{\partial C_i}{\partial t} = D \frac{\partial^2 C_i}{\partial x^2} - \frac{\partial C_p}{\partial t} \quad (3)$$

where  $C_i$  is the concentration of dissolved iron and  $C_p$  concentration of precipitated iron. Intra-granular precipitation of iron is assumed to be homogenous and is accounted for by the following equation:

$$\frac{\partial C_p}{\partial t} = 4\pi r_p^{IG} \overline{DN}_p^{IG} (C_i - C_{sol}) \quad (4)$$

where  $r_p^{IG}$  is the average precipitate radius in the intra-granular region, and is expressed here:

$$r_p^{IG} = \left( \frac{3 C_p}{4\pi \overline{N}_p^{IG} C_{Fe/FeSi_2}} \right)^{1/3} \quad (5)$$

Two boundary conditions are imposed, on each side of the domain representing the grain:

- On one side, a symmetry condition is set – i.e. no flux:

$$\frac{\partial C_i}{\partial x} = 0 \quad (6)$$

- Iron precipitation at the grain boundary is accounted for on the other side of the grain, by introducing the following flux  $J$  ( $cm^{-2}s^{-1}$ ):

$$J = \frac{1}{2} \frac{\partial C_s^{GB}}{\partial t} \quad (7)$$

where  $C_s^{GB}$  is the iron surficial concentration at the grain boundary interface. The “1/2” factor comes from the fact that only one side of the grain boundary is

considered in the model. The number of iron atoms flowing to a single precipitate per unit of time  $\Phi$  ( $s^{-1}$ ) is introduced. In the case where the distance between the precipitate is much larger than the precipitate radius,  $\Phi$  is expressed as follows [22]:

$$\Phi = 4\pi r_p^{GB} D (C_i^* - C_{sol}) \quad (8)$$

where  $C_i^*$  is, in the present case, the dissolved iron concentration at the grain boundary vicinity, and  $r_p^{GB}$  the average precipitate radius at the grain boundary. The time evolution of the surficial concentration of iron at the grain boundary interface is then:

$$\frac{\partial C_S^{GB}}{\partial t} = N_p^{GB} \Phi = 4\pi r_p^{GB} N_p^{GB} D (C_i^* - C_{sol}) \quad (9)$$

The average precipitate radius at the boundary is deduced from the following equation:

$$C_S^{GB} = N_p^{GB} C_{Fe/FeSi_2} \frac{4\pi}{3} (r_p^{GB})^3 \quad (10)$$

The set of parameters used for the simulations is listed in Table I.

**Table I.** Set of parameters used for the calculations. The iron supersaturation ratio  $k$  and the intra-granular density of precipitation sites  $N_p^{IG}$  values used for the evaluation of the average density of precipitation sites at grain boundary  $N_p^{GB}$  are added.

Parameter	Symbol	Value/Expression	Ref.
Fe diffusivity in Si(s)	D	$1.0 \times 10^{-3} \exp(-0.67\text{eV}/kT) \text{ cm}^2\text{s}^{-1}$	[23]
Fe solubility in Si(s)	$C_{sol}$	$1.8 \times 10^{26} \exp(-2.94\text{eV}/kT) \text{ cm}^3$	[23]
Fe atomic radius	$r_{at}$	$4.4 \times 10^{-8} \text{ cm}$	[22]
Fe concentration in FeSi <sub>2</sub>	$C_{Fe/FeSi_2}$	$2.5 \times 10^{22} \text{ cm}^{-3}$	[22]
Total iron concentration	$C_0$	$3.9 \times 10^{13} \text{ cm}^{-3}$	GDMS
Ingot cooling rate	CR	$-2.73 \times 10^{-2} \text{ K/s}$	
Iron supersaturation ratio	$k$	6300	Section IV.A
Intra-granular density of precipitation site	$N_p^{IG}$	$3.7 \times 10^8 \text{ cm}^{-3}$	Section IV.A

## IV. Results and Discussion

### A. Precipitation at Grain Boundaries

The total iron concentration in the wafer  $Fe_{tot}$  was measured by GDMS to be  $C_0 = 3.9 \times 10^{13} \text{ cm}^{-3}$  which is an order of magnitude above the detection limit of the instrument [20]. Figure 1(a) shows the map of dissolved iron of the studied wafer, as calculated using the FeB pair dissociation method. Two scales are added, one corresponding to the interstitial iron concentration  $Fe_i$ , and one to the ratio  $Fe_i / Fe_{tot}$ . This ratio corresponds to the part of dissolved iron over the total iron concentration, and is referred later as “dissolved iron ratio”. The average ratio value over the wafer is 0.10, and is added in red on the  $Fe_i / Fe_{tot}$  scale, in Figure 1(a). A sister wafer was selected for characterizing the grain structure using EBSD, and is shown in Figure 1(b).

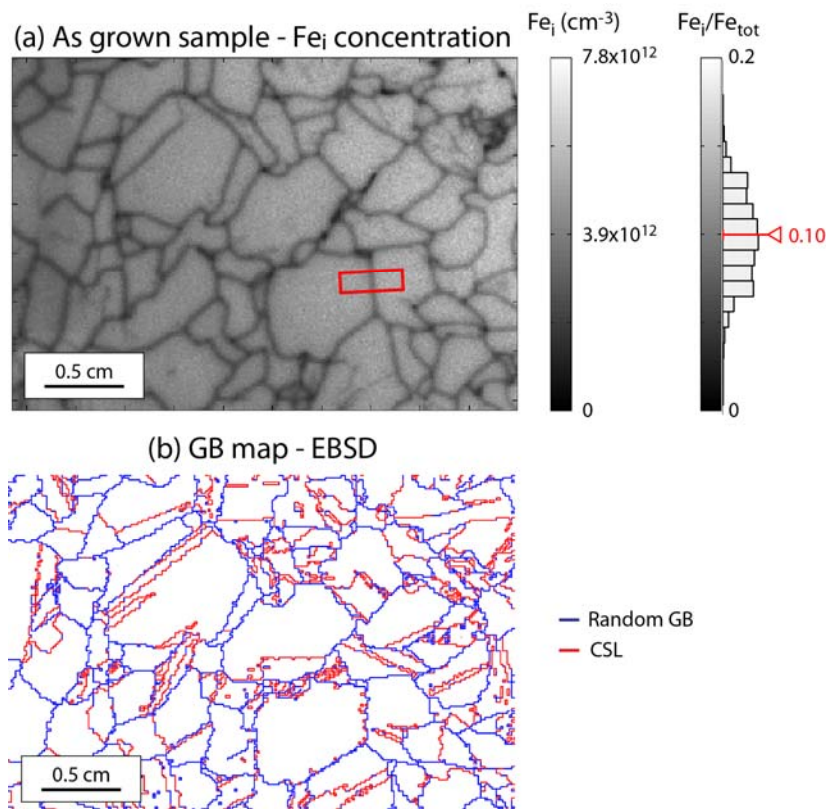


**Figure 1:** (a)  $Fe_i$  map obtained by PL-imaging using the FeB pair dissociation method. Two scales are added, one corresponding to the  $Fe_i$  concentration, and the other to the part of dissolved Fe, relatively to the total iron concentration  $Fe_{tot}$ , as measured by GDMS. The distribution and the average  $Fe_i / Fe_{tot}$  ratio are added on the second scale. The red box corresponds to the concentration profile plotted on Figure 4. (b) EBSD grain boundary map of the same wafer. A distinction is made between random grain boundaries (in blue), and coincidence site lattice (CSL) grain boundaries (in red).

The interstitial iron image showed in Figure 1(a) displays lines of dark contrast, corresponding to the active grain boundaries, i.e. the grain boundaries having the ability to precipitate iron. Thus, when performing a linescan on the interstitial iron map across an active grain boundary, a clear decrease of the

interstitial iron concentration is observed close to the boundary [24, 25]. These regions of lower concentration are commonly referred to as “depleted regions” or “denuded zones”, and indicate that iron has precipitated at the grain boundary during ingot cooling. An example of concentration profile, corresponding to the red box on Figure 1(a), is given in Figure 4. The interstitial iron concentrations were averaged over the vertical distance of the box.

When comparing Figure 1(a) and Figure 1(b), a clear correlation can be drawn between active grain boundaries and random angle grain boundaries. This comparison between grain boundary character and activity resembles the one previously made for steel, where active grain boundaries precipitate chromium, leaving denuded zones behind, and causing inter-granular corrosion. The identification of active grain boundaries in such materials has been the subject of many studies, and different criteria have been proposed to separate random grain boundaries from coincidence site lattice (CSL) grain boundaries [26-28]. These criteria define allowable angular deviations  $\Delta\theta$  from the perfect coincidence site lattice angle, as a function of the inverse density of coincident sites  $\Sigma$ . The more restrictive Palumbo’s criterion was identified in steel to be the one separating best active grain boundaries – i.e. random grain boundaries – from inactive ones – i.e. CSL grain boundaries [28]. The allowable angular deviation defined by Palumbo et al. is:

$$\Delta\theta = \frac{15}{(\Sigma)^{5/6}} \quad (11)$$

Similar conclusions are drawn in this work for the precipitation of iron in multicrystalline silicon. Figure 1(a) was compared to its associated grain boundary map, as given by EBSD, using in turn Brandon’s, Déchamps’ and Palumbo’s criteria. As for chromium in steel, the best separation was obtained for the Palumbo’s criterion, where 90% of the random grain boundaries and 10% of CSL grain boundaries were identified as being active.

Concentration profiles were extracted from Figure 1(a) across 32 active grain boundaries. Interstitial iron concentrations evaluated close to grain boundaries are likely to be influenced by lateral carrier diffusion occurring during PL imaging. This problem is discussed by Liu et al. in [29]. In order to obtain a better evaluation of the concentration at the grain boundary interface, the profiles were fitted with an error-function. An example is given in Figure 4. The average minority charge carrier lifetime over the studied wafer is 0.44  $\mu\text{s}$ , corresponding to an approximate diffusion length of 40  $\mu\text{m}$ . Lateral carrier diffusion impacts the calculated  $\text{Fe}_i$  concentrations close to grain boundaries over a distance of the same order of magnitude: Figure 3 shows that the deviation of the  $\text{Fe}_i$  data from the fit curve is the highest in the 100  $\mu\text{m}$  the closest to the grain boundary. In the current study, only the interstitial iron concentrations evaluated further from the grain boundary are trusted.

Lateral photon scattering occurring during PL measurements can also affect the  $\text{Fe}_i$  image calculated from the PL images taken before and after  $\text{FeB}$  pairs splitting. In order to assess the impact of this phenomenon on the  $\text{Fe}_i$  concentration profiles across the active grain boundaries, the studied sample was characterized using Micro-Photoluminescence ( $\mu\text{PL}$ ). This method is not

influenced by lateral photon scattering, as the PL signal is measured “pixel-by-pixel” [30]. The measured PL intensity map, which directly correlates with the minority charge carrier lifetime, is shown in Figure 2. Bright areas with higher contrast can be observed close to the grain boundaries. These are corresponding to the depleted regions of lower  $Fe_i$  concentrations described previously, and visible in Figure 1(a) [31]. The widths of the denuded zones are evaluated in the  $\mu$ PL image and the  $Fe_i$  image by fitting line-scans across active boundaries with an exponential decay function. The results are summarized in Table II.

**Table II.** Average widths of the denuded zones shown in the  $\mu$ PL and the  $Fe_i$  images.

	$\mu$ PL image	$Fe_i$ image
Average width ( $\mu\text{m}$ )	408 ( $\pm 80$ )	404 ( $\pm 44$ )

The average widths of the denuded zones in the  $Fe_i$  image and in the  $\mu$ PL image are very similar. The effect of lateral photon scattering on the  $Fe_i$  concentration profiles across active grain boundaries is therefore negligible, and the extrapolation given by the error function is believed to provide a good evaluation of the  $Fe_i$  concentration at the boundary interface.

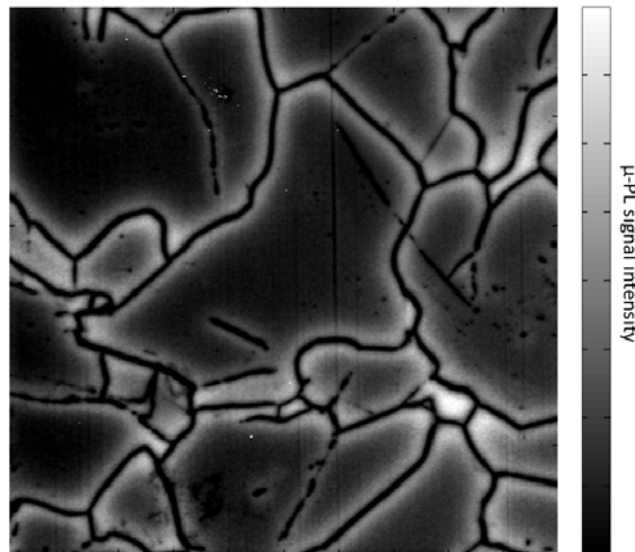


**Figure 2:** Micro-Photoluminescence ( $\mu$ PL) image of the sample. Depleted regions are visible at the active grain boundaries.

From the error-function fit, a “depletion-ratio”  $R_D$  was evaluated for each boundary, where

$$R_D = \frac{C_{int}}{C_\infty} \quad (12)$$

with  $C_{int}$  is the  $Fe_i$  concentration at the vicinity of the grain boundary, and  $C_\infty$  is the  $Fe_i$  concentration far from the grain boundary – i.e. bulk concentration. The results are summarized in Figure 3(b). A relatively homogeneous distribution of the depletion-ratio values is observed around an average of 0.63. This preliminary investigation suggests that, when a grain boundary precipitates iron, it does it with a remarkable homogeneous intensity.

Preliminary calculations have been performed using the *no-supersaturation assumption* – i.e. iron precipitation starts exactly when the temperature is low enough for the solubility limit to be overcome. An example is given in Figure 4, where both data and calculated profiles are added for a selected grain boundary (see red box on Figure 1(a)). A good estimation of the depletion ratio – i.e. the depth of the depleted region – is obtained for a surficial density of precipitation site  $N_p^{GB} = 4.1 \times 10^5 \text{ cm}^{-2}$ , but a deviation is observed between the data and the model, as the calculated profile exhibits a wider depleted region. This decay is the result of the *no-supersaturation assumption*, implying that precipitation starts too early during the cooling process, leaving more time for iron to precipitate and diffuse towards the boundary. It has been, however, shown in several studies that the onset of iron precipitation in silicon requires high supersaturation [32, 33]. In order to account for supersaturation, the “triggering temperature” was adjusted, so that the calculated depleted region width would fit to the measured one. The adjusted triggering temperature ( $T_t = 900\text{K}$ ) introduces a decay of 270 K from the supersaturation temperature ( $T_s = 1170 \text{ K}$ ), corresponding to a supersaturation ratio of  $k \sim 6300$ , where

$$k = \frac{C_0}{C_{sol}(T_t)} \quad (13)$$

This matter has been previously discussed by Liu et al. [29], where the authors estimated for their material an iron supersaturation ratio of 55. The much higher ratio evaluated in the present study is consistent with the much lower average dislocation densities present in HPMC-Si, relatively to standard multicrystalline silicon, resulting in lower densities of available precipitation sites. Higher supersaturation levels are therefore expected in HPMC-Si material to trigger iron precipitation.

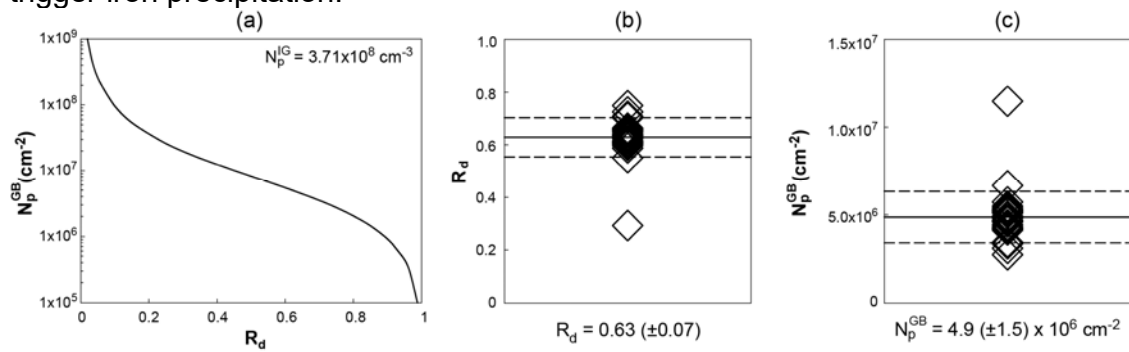


**Figure 3:** (a) Final depletion-ratio  $R_d$  as a function of the surficial density of precipitation sites at the boundary  $N_p^{GB}$ , as calculated by the 1D model, for the parameters listed in Annex I. (b) Depletion ratios  $R_d$ , as evaluated by extracting 32 concentration profiles across grain boundaries on Figure 1(a). An average value and the standard deviation are indicated. (c) Evaluated densities of precipitation sites at active grain boundaries. An average value and the standard deviation are indicated.

By using the 1D precipitation model presented before, an average surficial density of precipitation sites at active grain boundaries  $N_p^{GB}$  was evaluated. The intra-granular  $Fe_i$  concentration of each grain is directly measured on the iron interstitial map. An average intra-granular concentration of  $5.5 (\pm 0.7) \times 10^{12} \text{ cm}^{-3}$  is evaluated. From this value, and by using Equation (8), an intra-granular density of precipitation sites  $N_p^{IG}$  of approximately  $3.7 \times 10^8 \text{ cm}^{-3}$  is determined. This value is used for the 1D calculations.

An example of dissolved iron concentration profile time-evolution during the ingot cooling is displayed on Figure 5. The initial concentration level corresponds to the total iron concentration, as measured by GDMS. As the temperature decreases, iron precipitates, the dissolved intra-granular concentration decreases, and a depleted region forms close to the boundary interface. Diffusivity strongly limits iron precipitation at low temperatures, and almost no iron precipitates are found below 650 K. By adjusting the surficial density of precipitation sites at the boundary, a good fit is obtained between the final calculated concentration profile and the linescan performed on the iron interstitial image.

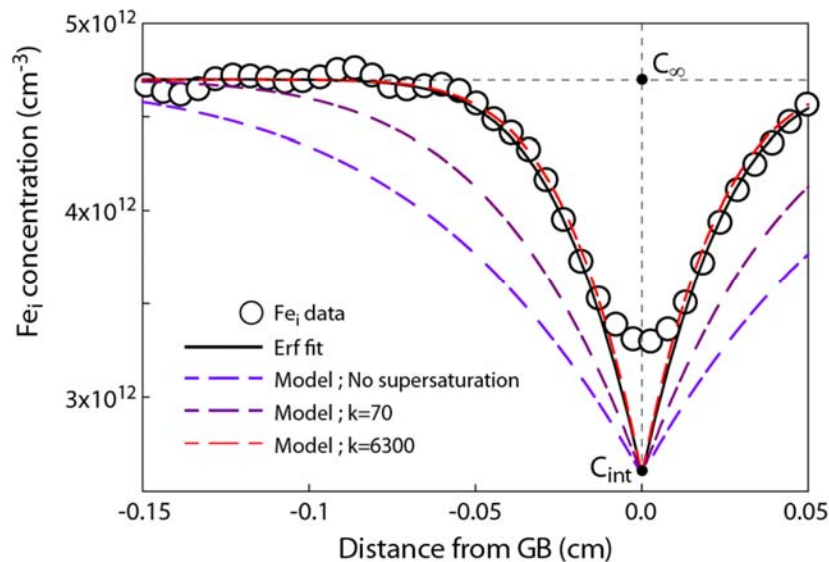


**Figure 4:** Example of  $Fe_i$  profile, as measured across a grain boundary on Figure 1(a). The data are fitted with an error function (Erf fit) in order to evaluate the interstitial iron concentration at the grain boundary interface ( $C_{int}$ ). The 1D model simulates the concentration profile, using the no-supersaturation assumption. A

good estimation of the depletion ratio is obtained by adjusting the surficial density of precipitation site  $N_p^{GB}$ , but a deviation is observed between the data and the model, as the calculated profile exhibits a wider depleted region. A good fit is obtained between the model and the  $Fe_i$  data when introducing a supersaturation ratio  $k=6300$ .

The calculations are repeated for a wide range of surficial density of precipitation site values. A power curve is obtained, giving the final depletion-ratio  $R_d$  as a function of the surficial density of precipitation sites at the boundary  $N_p^{GB}$  (see Figure 3(a)). It is important to note here that these calculations correspond to a specific set of parameters listed in Table I. From this curve and the previously measured depletion-ratios (Figure 3(b)), a set of surficial densities of precipitation site is evaluated (see Figure 3(c)). These values are homogeneously stacked around an average density of  $4.9 (\pm 1.5) \times 10^6 \text{ cm}^{-2}$ . The density of iron silicide precipitates at a random grain boundary was evaluated experimentally by Fenning et al. using X-ray fluorescence microscopy [34, 35]. The material studied by these authors contained a total iron concentration of  $\sim 1 \times 10^{14} \text{ cm}^{-3}$ . A precipitate density of  $1.5 \times 10^7 \text{ cm}^{-2}$  was measured at the boundary in as-cut material, where only precipitates with more than  $3 \times 10^4$  iron atoms were considered. This value is consistent with our evaluation.

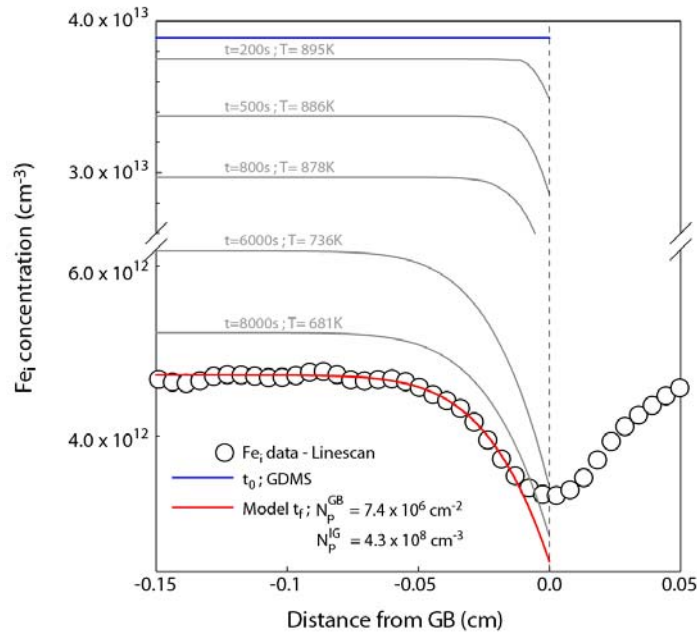


**Figure 5:** Example of the evolution of the dissolved iron concentration profile close to an active grain boundary, during the ingot cooling. The initial concentration corresponds to the total iron concentration, as measured by GDMS. Iron precipitation is triggered for a supersaturation ratio  $k = 6300$ , and intra-granular precipitation occurs as the bulk level of dissolved iron decreases. Grain boundary precipitation involves the development of a depleted region, close to the boundary interface.  $Fe_i$  data are added, corresponding to the red box

on Figure 1 (a). For a surficial density of precipitation site  $N_p^{GB} = 7.4 \times 10^6 \text{ cm}^{-2}$ , these data are well fitted by the model.

It is assumed in the 1D model that iron precipitates homogeneously in the intra-granular region. The density of dislocations can however be expected to vary from one grain to another, and within a single grain. A sensitivity study has therefore been performed to evaluate the dependence of the evaluated average density of precipitation sites at grain boundaries,  $N_p^{GB}$ , to the input intra-granular density of precipitation sites,  $N_p^{IG}$ . Figure 6(a) shows the surficial density of precipitation sites at the boundary,  $N_p^{GB}$ , plotted as a function of the calculated depletion-ratio  $R_d$ , for three different intra-granular density of precipitation sites  $N_p^{IG}$ . The standard case presented in Figure 3(a) – i.e.  $N_p^{IG} = 3.7 \times 10^8 \text{ cm}^{-3}$ , is shown on Figure 6(a), and two other cases are added,  $N_p^{IG} = 3.7 \times 10^7 \text{ cm}^{-3}$  and  $N_p^{IG} = 3.7 \times 10^9 \text{ cm}^{-3}$ . The average density of precipitation site at grain boundaries,  $N_p^{GB}$ , is evaluated for  $R_d = 0.63$  as a function of the intra-granular density of precipitation sites,  $N_p^{IG}$ . The results are plotted in Figure 6(b).

An estimated  $N_p^{GB}$  approximately two times higher than the one evaluated for  $N_p^{IG} = 3.7 \times 10^8 \text{ cm}^{-3}$  is obtained when considering an average  $N_p^{IG}$  an order of magnitude higher. Similarly, considering an average intra-granular density of precipitation site  $N_p^{IG}$  an order of magnitude lower results in an estimated  $N_p^{GB}$  only 1.4 times lower. A linear relationship between dislocation density and intra-granular density of precipitation site  $N_p^{IG}$  is commonly assumed [34, 35]. It is therefore believed that local variations of dislocation densities within a grain can safely be treated in the model by using the *homogeneous intra-granular precipitation assumption*, without affecting greatly the evaluation of  $N_p^{GB}$ .

A homogeneous intra-granular dislocation density of  $4.8 (\pm 1.5) \times 10^3 \text{ cm}^{-2}$  was evaluated across the wafer. A variation of intra-granular density of precipitation sites of  $\pm 30\%$  is consequently expected from one grain to another across the wafer. This variation corresponds to an evaluated  $N_p^{GB}$  ranging from  $4.4 \times 10^6 \text{ cm}^{-2}$  to  $5.1 \times 10^6 \text{ cm}^{-2}$  (Figure 6(b)). These values are very close to the  $N_p^{GB}$  evaluated for  $N_p^{IG} = 3.7 \times 10^8 \text{ cm}^{-3}$ , supporting once again the validity of the *homogeneous intra-granular precipitation assumption*.

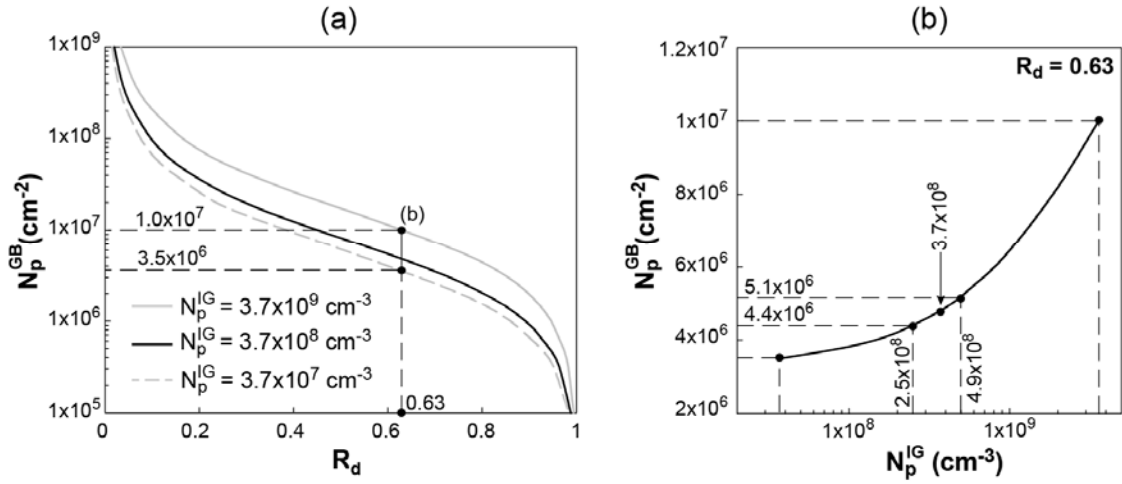


**Figure 6:** (a) Surficial density of precipitation sites at the boundary  $N_p^{GB}$  plotted as a function of the final depletion-ratio  $R_d$  for three different intra-granular densities of precipitation sites  $N_p^{IG}$ , namely  $3.7 \times 10^7$  cm<sup>-3</sup>,  $3.7 \times 10^8$  cm<sup>-3</sup>, and  $3.7 \times 10^9$  cm<sup>-3</sup>. The evaluated average depletion-ratio  $R_d=0.63$  is indicated. (b) Sensitivity curve showing the average density of precipitation site at grain boundaries  $N_p^{GB}$  calculated for  $R_d = 0.63$ , as a function of the intra-granular density of precipitation site  $N_p^{IG}$ .

## B. Area-averaged precipitation

The as-grown dissolved iron ratio has been calculated from Equation (1), for a range of area-averaged densities of precipitation sites. The results are plotted in Figure 7. As shown in Figure 1(a), the remaining interstitial iron concentration constitutes about 10% of the total iron concentration, corresponding to an area-averaged density of precipitation sites  $\overline{N_p} = 4.5 \times 10^8$  cm<sup>-3</sup>. The average intra-granular concentration was measured on the iron interstitial map to be  $5.5 (\pm 0.7) \times 10^{12}$  cm<sup>-3</sup> – corresponding to a dissolved iron ratio of 0.14. It should be noted here that the homogeneity of the intra-granular interstitial iron concentration across the studied wafer is consistent with a relatively homogeneous intra-granular dislocation density of  $4.8 (\pm 1.5) \times 10^3$  cm<sup>-2</sup>. Such low dislocation densities are expected to have very limited effect on the minority carrier diffusion length [36, 37]. The present results, however, show that such low dislocation densities can still drive iron to precipitate. The intra-granular dissolved iron ratio corresponds to an intra-granular density of precipitation sites of approximately  $3.7 \times 10^8$  cm<sup>-3</sup>, and therefore a linear density of precipitation sites at dislocations of  $7.7 \times 10^5$  cm<sup>-1</sup>. This latest value is consistent with the linear density of precipitation site at dislocations used in the work of Morishige et al. and Schön et al. [38, 39] – i.e.  $3.3 \times 10^5$  cm<sup>-1</sup>. The average intra-granular density of precipitation site –  $3.7 \times 10^8$  cm<sup>-3</sup> – is added on Figure 7, and

corresponds to a case where iron precipitation occurs exclusively in the intra-granular regions – i.e. precipitation at grain boundaries and dislocation clusters is discarded. Even though the average density of dislocations in the present material is low, the intra-granular density of precipitation sites is close to the area-averaged density of precipitation sites in the wafer, and almost the whole iron precipitation occurs in the intra-granular regions.

The average surficial density of precipitation sites at random grain boundaries was evaluated to be  $4.9 (\pm 1.5) \times 10^6 \text{ cm}^{-2}$  (see Figure 3(c)). From the EBSD map shown on Figure 1(b), the density of random grain boundaries across the studied wafer is evaluated to be approximately  $9.0 \text{ cm}^{-1}$ . The area-averaged density of precipitation site at grain boundaries across the wafer is then  $\bar{N}_p = 4.4 \times 10^7 \text{ cm}^{-3}$ . This value is added on Figure 7, and corresponds to a case where iron precipitation occurs exclusively at the grain boundaries – i.e. precipitation in the intra-granular regions and dislocation clusters is discarded. In this case the value of the dissolved iron ratio is close to 1, and grain boundaries have relatively limited impact on iron precipitation.

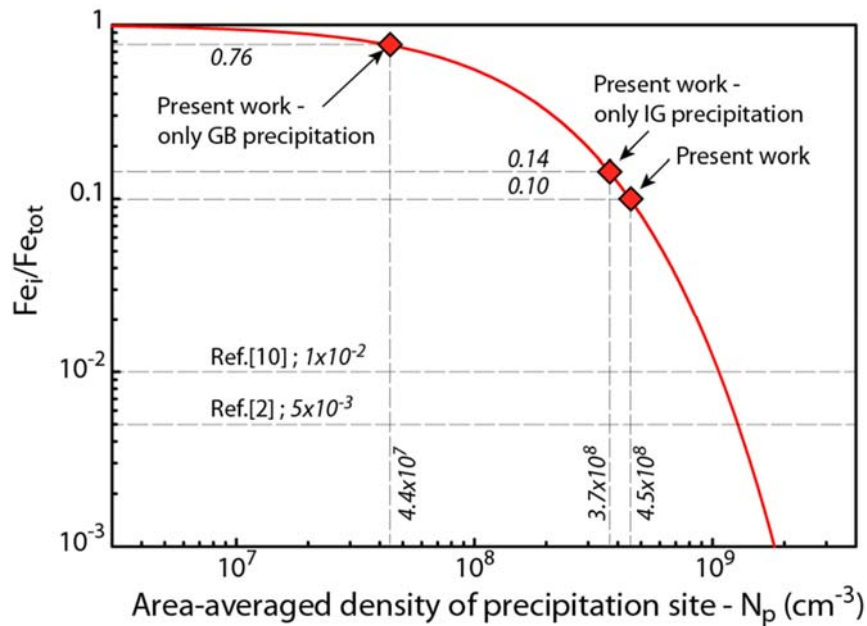


**Figure 7:** Ratio of dissolved iron at the end of the solidification process, as a function of the area averaged density of precipitation sites, as calculated from Equation (1). The dissolved iron ratio corresponding to the present work is 0.10. The isolated effect of intra-granular (IG) precipitation and grain boundary (GB) precipitation is added on the graph. Previous ratios obtained by Macdonald et al. [10] and Istratov et al. [2] are added for qualitative comparison.

Ratios between dissolved and total iron contents have been previously reported by Macdonald et al. [10] and Istratov et al. [2]. These values are more than one order of magnitude lower than the one presented in this work, and are added on Figure 7.

The material investigated in the present study has been obtained from a multi-seeded growth process, resulting in the solidification of a so-called high-performance multicrystalline silicon (HPMC-Si) ingot. As mentioned in the introduction, this technique favors the growth of a more random structure, characterized by a limited development of dislocation clusters [13]. The lower density of dislocation clusters in HPMC-Si leads to a limited precipitation of iron, as the density of available precipitation sites is lower than in standard multicrystalline silicon. The difference between the dissolved iron ratio evaluated by Macdonald et al. and Istratov et al., and the one obtained in the present study clearly illustrates the important effect of dislocation clusters on iron precipitation.

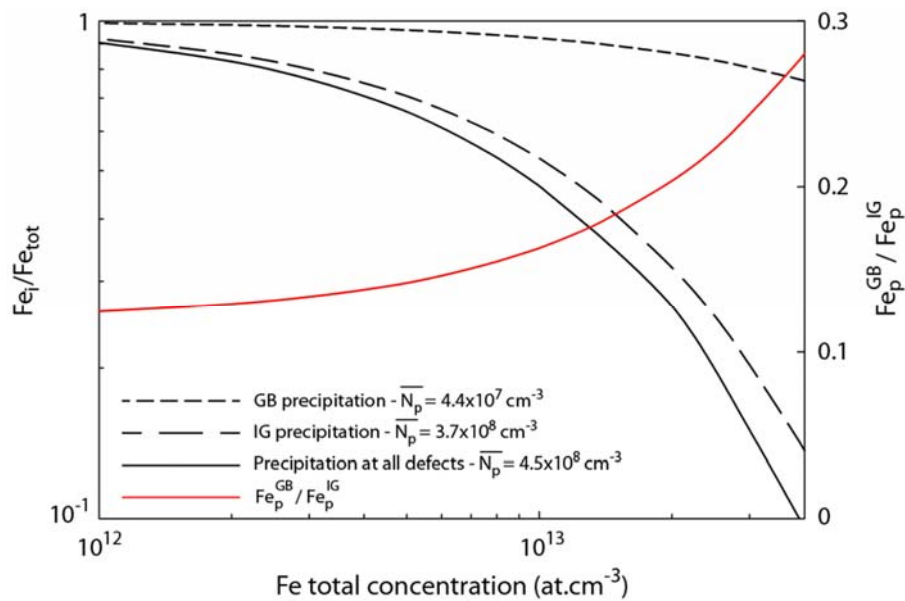


**Figure 8:** Ratio of dissolved iron at the end of the solidification process, as a function of the total iron concentration. Three cases are presented, showing the separated effect of grain boundary (GB) and intra-granular (IG) precipitation, and the combined effect of all structural defects.

The studied material was taken at ~80% ingot height. This relatively high position in the ingot was selected in order to (1) obtain clear depleted regions close to the grain boundaries on the  $Fe_i$  map, and (2) measure the total iron concentration with GDMS. The iron levels in the present material are an order of magnitude higher than the iron concentration found in the center of the ingot. In order to discuss the influence of the total concentration of iron on the results presented in this work, the as-grown ratio of dissolved iron was calculated as a function of the total iron concentration. It is assumed that the grain structure does not change over height – i.e. the average precipitation site densities used for the calculations are the ones evaluated in section IV.A – and the same ingot-cooling rate CR was utilized. The supersaturation ratio is also assumed not vary with the total iron concentration. The results are plotted in Figure 8. Three separated cases are displayed, showing the sole effects of grain boundary and intra-granular precipitation, and the combined effect of all structural defects. A fourth

curve is added (in red), corresponding to the ratio between the precipitated iron at grain boundaries and intra-granular dislocations.

The limited effect of grain boundaries on iron precipitation is still valid for lower iron concentrations, and most of precipitation still occurs at intra-granular dislocations. The final dissolved iron ratios are furthermore closer to one for lower concentrations, and only ~10% of the iron is expected to precipitate for total concentrations in the order of  $10^{12} \text{ cm}^{-3}$ . The relatively lower ability of HPMC-Si material to precipitate iron is then even more remarkable in the low iron concentration range.

## V. Summary - Conclusion

A study of the spatial occurrence of iron precipitation in HPMC-Si material has been conducted. By examining the depleted region width developing close to the grain boundaries, a supersaturation ratio  $k \sim 6300$  has been estimated. This value is much higher than the previous value reported in literature for standard multicrystalline material. This difference is attributed to the lower density of precipitation sites available in HPMC-Si compared to standard mc-Si, due to the relatively low dislocation density. Active grain boundaries are mostly identified as random angle grain boundaries and an examination of their depleted ratio showed that they precipitate iron with a relatively homogeneous intensity. An average surficial density of precipitation sites at active grain boundaries  $N_p^{\text{GB}} = 4.9 (\pm 1.5) \times 10^6 \text{ cm}^{-2}$  has been evaluated, which is consistent with values from literature.

The area-averaged fraction of dissolved iron  $\text{Fe}_i / \text{Fe}_{\text{tot}}$  in the studied HPMC-Si material is more than an order of magnitude higher than ratios estimated in previous work for standard material. This observation is associated to the relatively lower density of dislocation clusters found in HPMC-Si and indicates that grain growth control has led to a clear decrease of iron precipitation in multicrystalline materials.

However, even though dislocations are present in HPMC-Si in relatively low densities, they prove to still be active in terms of iron precipitation. The separated effect of grain-boundaries, sparse intra-granular dislocations, and dislocation clusters on iron precipitation was investigated. It is shown that almost the entire iron precipitation occurs in the intra-granular regions and that the contribution of grain boundary precipitation is surprisingly low, despite the comparably small grain sizes in HPMC-Si.

## VI. Acknowledgement

The main research activity for this publication has been performed in the project *Impurity Control in High Performance Multicrystalline Silicon*, supported by the Research Council of Norway under the contract 228930/E20, REC Silicon, REC Solar, Steuler Solar and The Quartz Corp. The authors would like to thank the European Community for funding in the frame of the SOPHIA project (7FP7-

SOPHIA grant agreement n ° 262533), which financed the measurements of dissolved iron. The investigated material was made in the Norwegian Research Centre for Solar Cell Technology (*FME-Solar United*), also financed by the Research Council of Norway and several industrial partners.

## VII. References

- [1] A. A. Istratov, H. Hieslmair, E.R. Weber, Iron contamination in silicon technology, *Applied Physics A: Materials Science and Processing*, **70**, 489 (2000).
- [2] A. A. Istratov, T. Buonassisi, R.J. McDonald, A.R. Smith, R. Schindler, J.A. Rand, J.P. Kalejs, E.R. Weber, Metal content of multicrystalline silicon for solar cells and its impact on minority carrier diffusion length, *Journal of Applied Physics*, **94**, 6552 (2003).
- [3] M. C. Schubert, J. Schon, F. Schindler, W. Kwapil, A. Abdollahinia, B. Michl, S. Riepe, C. Schmid, M. Schumann, S. Meyer, W. Warta, Impact of impurities from crucible and coating on mc-silicon quality-The example of iron and cobalt, *IEEE Journal of Photovoltaics*, **3**, 1250 (2013).
- [4] F. Schindler, B. Michl, J. Schon, W. Kwapil, W. Warta, M.C. Schubert, Solar Cell Efficiency Losses Due to Impurities From the Crucible in Multicrystalline Silicon, *IEEE Journal of Photovoltaics*, **4**, 129 (2014).
- [5] R. Kvande, L. J. Geerligs, G. Coletti, L. Arnberg, M. Di Sabatino, E. J. Øvrelid, C. C. Swanson., Distribution of iron in multicrystalline silicon ingots, *Journal of Applied Physics*, **104**, 064905 (2008).
- [6] G. Coletti, Impurities in silicon and their impact on solar cell performance, PhD thesis, Universiteit Utrecht, 2011.
- [7] T. Buonassisi, A. A. Istratov, M.D. Pickett, J.P. Rakotoniaina, O. Breitenstein, M.A. Marcus, S.M. Heald, E.R. Weber, Transition metals in photovoltaic-grade ingot-cast multicrystalline silicon: Assessing the role of impurities in silicon nitride crucible lining material, *Journal of Crystal Growth*, **287**, 402 (2006).
- [8] T. Buonassisi, A. A. Istratov, M.D. Pickett, M. Heuer, J.P. Kalejs, G.Hahn, M.A. Marcus, B. Lai, Z. Cai, S.M. Heald, T.F. Ciszek, R.F. Clark, D.W. Cunningham, A.M. Gabor, R. Jonczyk, S. Narayanan, E. Saunar, E.R. Weber, Chemical natures and distributions of metal impurities in multicrystalline silicon materials, *Progress in Photovoltaics: Research and Applications*, **14**, 513 (2006).
- [9] T. Buonassisi, A. A. Istratov, M. Heuer, M. A. Marcus, R. Jonczyk, J. Isenberg, B. Lai, Z. Cai, S. Heald, W. Warta, R. Schindler, G. Willeke, E. R. Weber, Synchrotron-based investigations of the nature and impact of iron contamination in multicrystalline silicon solar cells, *Journal of Applied Physics*, **97**, 074901 (2005).
- [10] D. Macdonald, A. Cuevas, A. Kinomura, Y. Nakano, L.J. Geerligs, Transition-metal profiles in a multicrystalline silicon ingot, *Journal of Applied Physics*, **97**, 033523 (2005).

- [11] D. P. Fenning, J. Hofstetter, M.I. Bertoni, G. Coletti, B. Lai, C. del Cañizo, T. Buonassisi, Precipitated iron: A limit on gettering efficacy in multicrystalline silicon, *Journal of Applied Physics*, **113**, 044521 (2013).
- [12] C. W. Lan, W.C. Lan, T.F. Lee, A. Yu, Y.M. Yang, W.C. Hsu, B. Hsu, A. Yang, Grain control in directional solidification of photovoltaic silicon, *Journal of Crystal Growth*, **360**, 68 (2012).
- [13] Y. M. Yang, A. Yu, W.C. Hsu, B. Hsu, C. W. Lan, Development of high-performance multicrystalline silicon for photovoltaic industry, *Progress in Photovoltaics: Research and Applications*, **23**, 340 (2015).
- [14] G. Stokkan, Y. Hu, Ø. Mjøs, M. Juel, Study of evolution of dislocation clusters in high performance multicrystalline silicon, *Solar Energy Materials and Solar Cells*, **130**, 679 (2014).
- [15] B. L. Sopori, A New Defect Etch for Polycrystalline Silicon, *Journal of The Electrochemical Society*, **131**, 667 (1984).
- [16] D. Macdonald, J. Tan, T. Trupke, Imaging interstitial iron concentrations in boron-doped crystalline silicon using photoluminescence, *Journal of Applied Physics*, **103**, 073710 (2008).
- [17] M. C. Schubert, H. Habenicht, W. Warta, Imaging of Metastable Defects in Silicon, *IEEE Journal of Photovoltaics*, **1**, 168 (2011).
- [18] T. Trupke, R. A. Bardos, M. C. Schubert, W. Warta, Photoluminescence imaging of silicon wafers, *Applied Physics Letters*, **89**, 044107 (2006).
- [19] J. A. Giesecke, M. C. Schubert, B. Michl, F. Schindler, W. Warta, Minority carrier lifetime imaging of silicon wafers calibrated by quasi-steady-state photoluminescence, *Solar Energy Materials and Solar Cells*, **95**, 1011 (2011).
- [20] M. Di Sabatino, Detection limits for glow discharge mass spectrometry (GDMS) analyses of impurities in solar cell silicon, *Measurement*, **50**, 135 (2014).
- [21] F. S. Ham, Theory of diffusion-limited precipitation, *Journal of Physics and Chemistry of Solids*, **6**, 335 (1958).
- [22] C. Del Cañizo, A. Luque, Comprehensive model for the gettering of lifetime-killing impurities in silicon, *Journal of The Electrochemical Society*, **147**, 2685 (2000).
- [23] A. A. Istratov, H. Hieslmair, E.R Weber, Iron and its complexes in silicon, *Applied Physics A*, **69**, 13 (1999).
- [24] A. Liu, *et al.*, "Investigating internal gettering of iron at grain boundaries in multicrystalline silicon via photoluminescence imaging," *IEEE Journal of Photovoltaics*, vol. 2, pp. 479-484, 2012.
- [25] A. Liu, D. Macdonald, Precipitation of iron in multicrystalline silicon during annealing, *Journal of Applied Physics*, **115**, (2014).
- [26] D. G. Brandon, The structure of high-angle grain boundaries, *Acta Metallurgica*, **14**, 1479 (1966).
- [27] M. Déchamps, F. Baribier, A. Marrouche, Grain-boundaries: Criteria of specialness and deviation from CSL misorientation, *Acta Metallurgica*, **35**, 101 (1987).

- [28] G. Palumbo, K.T. Aust, E.M. Lehockey, U. Erb, P. Lin, On a More Restrictive Geometric Criterion for “Special” CSL Grain Boundaries, *Scripta Materialia*, **38**, 1685 (1998).
- [29] A. Liu, D. Walter, P. Sieu Pheng, D. Macdonald, Investigating internal gettering of iron at grain boundaries in multicrystalline silicon via photoluminescence imaging, *IEEE Journal of Photovoltaics*, **2**, 479 (2012).
- [30] F.D. Heinz, L.E. Mundt, W. Warta, M.C. Schubert, A Combined Transient and Steady State Approach for Robust Lifetime Spectroscopy with Micrometre Resolution, *Physica Status Solidi - Rapid Research Letters*, **9**, 697, 2015
- [31] M. Knörlein, A. Autruffe, R. Søndena, M. Di Sabatino, Internal gettering of iron at extended defects, *Energy Procedia*, **55**, 539 (2014).
- [32] A. Haarahiltunen, H. Väinölä, O. Anttila, M. Yli-Koski, J. Sinkkonen, Experimental and theoretical study of heterogeneous iron precipitation in silicon, *Journal of Applied Physics*, **101**, 043507 (2007).
- [33] D. A. Ramappa, W. B. Henley, Stability of iron-silicide precipitates in silicon, *Journal of The Electrochemical Society*, **144**, 4353 (1997).
- [34] D. P. Fenning, J. Hofstetter, M. I. Bertoni, S. Hudelson, M. Rinio, J. F. Lelièvre, B. Lai, C. del Cañizo, T. Buonassisi, Iron distribution in silicon after solar cell processing: Synchrotron analysis and predictive modeling, *Applied Physics Letters*, **98**, 162103 (2011).
- [35] J. Schön, A. Haarahiltunen, H. Savin, D. P. Fenning, T. Buonassisi, W. Warta, M. C. Schubert, Analyses of the Evolution of Iron-Silicide Precipitates in Multicrystalline Silicon During Solar Cell Processing, *IEEE J. of Photovoltaics*, **3**, 131-137 (2013).
- [36] M. Rinio, S. Peters, M. Werner, A. Lawrenz, H.J. Möller, Measurement of the normalized recombination strength of dislocations in multicrystalline silicon solar cells, *Solid State Phenomena*, **82**, 701 (2002).
- [37] C. Donolato, Modeling the effect of dislocations on the minority carrier diffusion length of a semiconductor, *Journal of Applied Physics*, **84**, 2656 (1998).
- [38] A. Morishige, Hannu S. Laine, Jonas Schön, Antti Haarahiltunen, Jasmin Hofstetter, Carlos del Cañizo, Martin C. Schubert, Hele Savin, Tonio Buonassisi, Building intuition of iron evolution during solar cell processing through analysis of different process models, *Applied Physics A*, **120**, 1357 (2015).
- [39] J. Schön, H. Habenicht, M.C. Schubert, W.Warta, Understanding the distribution of iron in multicrystalline silicon after emitter formation: Theoretical model and experiments, *Journal of Applied Physics*, **109**, 063717 (2011).